

# Forecasting Constraint on Primordial Black Hole Properties with the CSST $3 \times 2$ pt Analysis

DINGAO HU <sup>1,2</sup> YAN GONG <sup>1,2,3</sup> PENGFEI SU,<sup>1,2</sup> HENGJIE LIN <sup>1</sup> HAITAO MIAO <sup>1</sup> QI XIONG <sup>1,2</sup> AND  
XUELEI CHEN <sup>1,2,4,5,6</sup>

<sup>1</sup>*National Astronomical Observatories, Chinese Academy of Sciences, 20A Datun Road, Beijing 100101, China*

<sup>2</sup>*School of Astronomy and Space Sciences, University of Chinese Academy of Sciences(UCAS),  
Yuquan Road NO.19A Beijing 100049, China*

<sup>3</sup>*Science Center for Chinese Space Station Survey Telescope, National Astronomical Observatories,  
Chinese Academy of Science, 20A Datun Road, Beijing 100101, China*

<sup>4</sup>*Department of Physics, College of Sciences, Northeastern University, Shenyang 110819, China*

<sup>5</sup>*Centre for High Energy Physics, Peking University, Beijing 100871, China*

<sup>6</sup>*State Key Laboratory of Radio Astronomy and Technology, China*

## ABSTRACT

This study forecasts the constraints on the properties of primordial black holes (PBHs) as a cold dark matter component using the galaxy clustering, weak lensing, and galaxy-galaxy lensing (i.e.  $3 \times 2$ pt) measurements from the upcoming Chinese Space Station Survey Telescope (CSST) photometric survey. Since PBHs formed via gravitational collapse in the early Universe, they can additionally affect the formation and evolution of the cosmic large-scale structure (LSS) through “Poisson” effect. We compute the angular power spectra for PBH- $\Lambda$ CDM cosmology, and generate mock data based on the CSST instrumental and survey design. The Markov Chain Monte Carlo (MCMC) method is employed to constrain the free parameters, such as the product of the PBH fraction and mass  $f_{\text{PBH}}m_{\text{PBH}}$  and other cosmological parameters. The systematic parameters are also included in the fitting process, such as the parameters of baryonic effect, intrinsic alignment, galaxy bias, photometric redshift (photo- $z$ ) calibration, shear calibration, and noise terms. We find that the CSST  $3 \times 2$ pt analysis can achieve tight constraints on  $f_{\text{PBH}}m_{\text{PBH}}$ , with 68% and 95% confidence levels (CLs) reaching  $< 10^{3.9} M_{\odot}$  and  $< 10^{4.7} M_{\odot}$ , respectively. Additionally, the cosmological parameters, e.g.  $\Omega_m$ ,  $\sigma_8$  and  $w$ , can be constrained with the precisions of 3.3%, 1.7%, 13%, respectively. This indicates that the CSST  $3 \times 2$ pt analysis is a powerful tool to advance the PBH dark matter studies in the near future.

**Keywords:** Primordial black holes (1292) — Cosmological parameters (339) — Large-scale structure of the universe (902) — Dark matter (353)

## 1. INTRODUCTION

Primordial black holes (PBHs) are believed to form through gravitational collapse of large overdensity regions in the early Universe. Various theories describe the PBH formation, including inhomogeneities during the radiation-dominated era (B. J. Carr 1975), critical collapse (F. Kühnel et al. 2016; B. Carr et al. 2021a), etc. Depending on the PBH formation time from  $10^{-43}$  to 1 s, the PBH mass ranges from  $10^{-5}$  gram to  $10^5 M_{\odot}$ . In some theories, the mass of PBHs can even extend to  $10^{22} M_{\odot}$  (B. J. Carr & A. M. Green 2024). Due to

their early formation and wide mass range, PBHs can explain various observational effects as cold dark matter (CDM), such as the coherence between the cosmic infrared background and unresolved cosmic X-ray background (A. Kashlinsky et al. 2025), the UV luminosity density of James Webb Space Telescope (JWST) (A. Matteri et al. 2025), etc. Different methods are used to constrain the properties of PBHs for different mass ranges, including  $\gamma$ -ray background (A. Arbey et al. 2020) and anisotropies of cosmic microwave background (CMB) (P. D. Serpico 2024) for small-mass PBHs, microlensing for solar-mass PBHs (B. Carr et al. 2021b), and dynamical motions and cosmic large-scale structure (LSS) for large-mass PBHs (C. Byrnes et al. 2025).

The combination of galaxy clustering and cosmic shear measurements, i.e.  $3 \times 2$ pt, is a powerful probe for the LSS, which is widely used to constrain the cosmological parameters (W. Hu & B. Jain 2004; D. E. S. Collaboration et al. 2022), including the Kilo-Degree Survey (KiDS) (B. Stolzner et al. 2025; A. H. Wright et al. 2025), Dark Energy Survey (DES) (T. Abbott et al. 2018; D. E. S. Collaboration et al. 2022), Hyper Suprime-Cam (HSC) (S. More et al. 2023; S. Sugiyama et al. 2023), etc. Especially, the upcoming Stage IV surveys can cover larger redshift range and sky area, and will constrain cosmological parameters more tightly, include the Chinese Space Station Survey Telescope (CSST) (H. Zhan 2011, 2021; Y. Gong et al. 2019, 2025; C. Collaboration et al. 2025), Vera Rubin Observatory’s Legacy Survey of Space and Time (LSST) (Z. Ivezić et al. 2019), *Euclid* (E. Collaboration et al. 2025a,b), and Nancy Grace Roman Space Telescope (RST) (J. Green et al. 2012).

In this work, we use the CSST  $3 \times 2$ pt probe to constrain the PBH properties. The CSST is a 2-meter space telescope and will co-orbits with the China Manned Space Station. It is planned to launch around 2027, and will cover a sky area of  $17500 \text{ deg}^2$  in about ten years with field of view of  $1.1 \text{ deg}^2$ . The CSST can effectively constrains the dark energy and dark matter properties (Y. Gong et al. 2019; Q. Xiong et al. 2024; H. Miao et al. 2024; Y. Song et al. 2024a,b), neutrino mass (H. Lin et al. 2022), ultralight axions (H. Lin et al. 2024), modified gravity models (A. Chen et al. 2022; J.-H. Yan et al. 2024), etc. The great observational ability of the CSST will also has significant potential for constraining the PBH properties.

The paper is organized as follows : in Section 2, we discuss the PBH effects in cosmology and the theory of angular power spectra for galaxy clusters and cosmic shear; in Section 3, we introduce the method of generating and selecting the mock data of angular power spectra; in Section 4, we discuss the  $3 \times 2$ pt fitting method and constraint results of the free parameters; Section 5 gives the summary and relevant discussions. We assume a flat  $\Lambda$ CDM cosmology with the fiducial values of the cosmological parameters from *Planck* measurements (P. Collaboration et al. 2020).

## 2. THEORETICAL MODEL

### 2.1. PBH- $\Lambda$ CDM Power Spectrum

PBHs can be seen as a component of CDM, and could cause specific effects on structure formation through their isocurvature perturbations. Therefore, the properties of PBHs can be constrained by the measurements of cosmic structure formation. The influence of PBHs can be specifically categorized into two types: “Poisson”

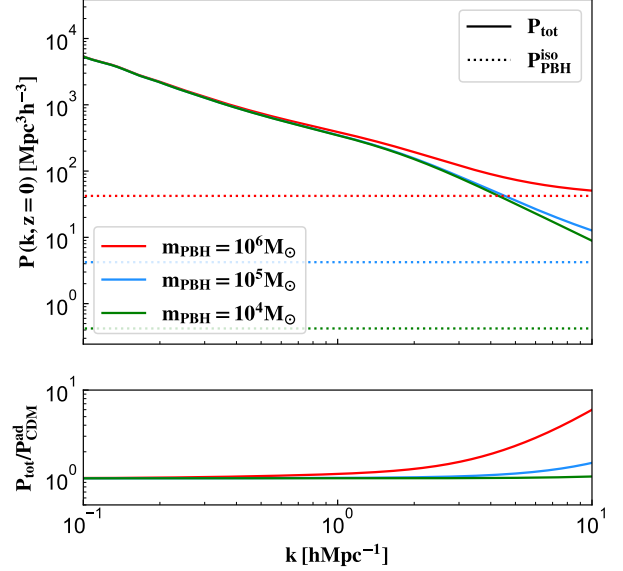


**Figure 1.** The total PBH- $\Lambda$ CDM power spectra (solid curves) and PBH isocurvature power spectra (dotted lines) in the PBH- $\Lambda$ CDM model at  $z = 0$  with  $f_{\text{PBH}} = 1$  for the three PBH masses, i.e.  $m_{\text{PBH}} = 10^4$  (green),  $10^5$  (blue), and  $10^6 M_{\odot}$  (red). The ratio of the PBH- $\Lambda$ CDM and  $\Lambda$ CDM matter power spectrum for each  $m_{\text{PBH}}$  is also shown in the lower panel.

effect and “Seed” effect. The “Poisson” effect represents the collective influence of multiple PBHs coexisting within a given region, and the “Seed” effect represents the isolated influence of a single PBH within a given region (B. Carr & J. Silk 2018). Since there is still no reliable model to accurately describe the “Seed” effect, we only focus on the “Poisson” effect in this work. Regarding the mass spectrum of PBHs, it has shown that constraints on a monochromatic mass spectrum can be extended to arbitrary mass spectra (B. Carr et al. 2017). Therefore, in this work, we assume that PBHs have a monochromatic mass spectrum.

Under these assumptions, the initial matter power spectrum for PBH isocurvature perturbations is given by (N. Afshordi et al. 2003)

$$P_{\text{PBH}}^{\text{iso}} = f_{\text{PBH}}^2 \bar{n}_{\text{PBH}}^{-1} = \frac{8\pi G f_{\text{PBH}} m_{\text{PBH}}}{3H_0^2 \Omega_{\text{CDM}}}, \quad (1)$$

where  $f_{\text{PBH}}$  is the PBH fraction of CDM,  $m_{\text{PBH}}$  is the mass of a single PBH, and  $\bar{n}_{\text{PBH}}$  is the mean volume number density of PBHs in comoving coordinate system. Since  $f_{\text{PBH}}$  and  $m_{\text{PBH}}$  are completely degenerate, the product  $f_{\text{PBH}} m_{\text{PBH}}$  is treated as a free parameter in our analysis.  $\Omega_{\text{CDM}} = \Omega_m - \Omega_b$  is the CDM density parameter, where  $\Omega_m$  and  $\Omega_b$  are the matter and baryon density parameters, respectively. The gravitational constant is  $G = 6.67 \times 10^{-11} \text{ m}^3 \text{ kg}^{-1} \text{ s}^{-2}$  and the Hubble parameter

is  $H_0 \equiv 100 h \text{ km s}^{-1} \text{ Mpc}^{-1}$  with  $h = 0.6727$ . Note that the power spectrum of the PBH adiabatic perturbation  $P_{\text{PBH}}^{\text{ad}}$  is identical to that of ordinary CDM, which can be absorbed into the matter power spectrum  $P_{\text{CDM}}^{\text{ad}}$  of the standard  $\Lambda\text{CDM}$  (N. Afshordi et al. 2003; D. Inman & Y. Ali-Haimoud 2019).

Considering the evolution of PBH isocurvature perturbations and the  $\Lambda\text{CDM}$  standard adiabatic model, the total power spectrum of the PBH- $\Lambda\text{CDM}$  cosmology can be expressed as

$$P_{\text{tot}}(k, z) = P_{\text{CDM}}^{\text{ad}}(k, z) + D^{\text{iso}}(z)^2 P_{\text{PBH}}^{\text{iso}}, \quad (2)$$

where  $D^{\text{iso}}(z)$  is the growth factor for PBH isocurvature perturbations, follows the expression as below (D. Inman & Y. Ali-Haimoud 2019)

$$D^{\text{iso}}(z) \approx (1 + \frac{3\gamma}{2\alpha_-} s)^{\alpha_-}, \quad s = \frac{1 + z_{\text{eq}}}{1 + z}, \quad (3)$$

$$\alpha_- = \frac{1}{4}(\sqrt{1 + 24\gamma} - 1), \gamma = \frac{\Omega_{\text{CDM}}}{\Omega_m},$$

where  $z_{\text{eq}} = 3400$  is the redshift at matter-radiation equality. Since PBHs mainly affect the cosmic structures at small scales, we estimate the non-linear matter power spectrum  $P_{\text{CDM}}^{\text{ad}}(k, z)$  by using CAMB (A. Lewis et al. 2000) with HMCode-2020 (A. Mead et al. 2021).

In Figure 1, we show the total (solid) and PBH (dotted) isocurvature perturbations power spectra in the PBH- $\Lambda\text{CDM}$  cosmology for  $m_{\text{PBH}} = 10^4, 10^5$ , and  $10^6 M_{\odot}$  with  $f_{\text{PBH}} = 1$  at  $z = 0$ . We can find that the PBH power spectrum is a constant for each  $m_{\text{PBH}}$ , and can significantly affect the total power spectrum at small scales of the non-linear regime with  $k \gtrsim 0.7$  and  $4 \text{ Mpc}^{-1} h$  for  $m_{\text{PBH}} = 10^6$  and  $10^5 M_{\odot}$ , respectively.

## 2.2. Galaxy Angular Power Spectrum

After obtaining the total matter power spectrum in the PBH- $\Lambda\text{CDM}$  cosmology, we can estimate the galaxy angular auto- or cross-power spectrum for the  $i$ -th and  $j$ -th tomographic redshift bins, which is given by

$$\tilde{C}_{\text{gg}}^{ij} = C_{\text{gg}}^{ij} + \frac{\delta_{ij}}{\bar{n}_{\text{g}}^i} + N_{\text{sys}}^{\text{g}}. \quad (4)$$

Here  $\delta_{ij}/\bar{n}_{\text{g}}^i$  represents the shot noise term, where  $\delta_{ij}$  is Kronecker delta function and  $\bar{n}_{\text{g}}^i$  is the mean galaxy surface number density in the  $i$ -th bin.  $N_{\text{sys}}^{\text{g}}$  denotes the systematic error term, which is simply assumed to be independent of bins or scales and can be seen as an average value, and we take  $N_{\text{sys}}^{\text{g}} = 10^{-8}$  as the fiducial value (Y. Gong et al. 2019). The quantity  $C_{\text{gg}}^{ij}$  is the clustering term of the galaxy angular power spectrum.

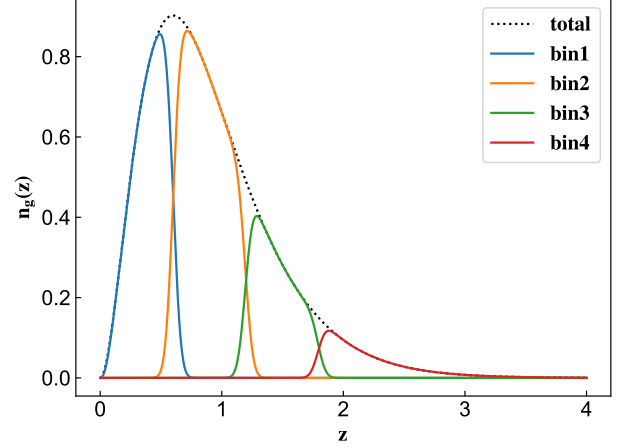


**Figure 2.** The adopted galaxy redshift distributions in the CSST photometric survey. The black dotted curve shows the normalized total galaxy redshift distribution  $n_{\text{g}}(z)$ , and the blue, orange, green, and red curves denote the galaxy redshift distribution in the four tomographic bins.

Using the flat sky assumption and Limber approximation (D. N. Limber 1954), it can be computed as (W. Hu & B. Jain 2004)

$$C_{\text{gg}}^{ij}(\ell) = \int dz H(z) \frac{W_{\text{g}}^i(z) W_{\text{g}}^j(z)}{c D_{\text{A}}^2(z)} P_m \left( \frac{\ell + \frac{1}{2}}{D_{\text{A}}(z)}, z \right), \quad (5)$$

where  $c$  is the speed of light,  $H(z)$  is the Hubble parameter,  $D_{\text{A}}$  is the comoving angular diameter distance,  $P_m(k, z) = P_{\text{tot}}(k, z)$  is the total matter power spectrum in the PBH- $\Lambda\text{CDM}$  cosmology in our analysis.  $W_{\text{g}}^i(z)$  is the galaxy weight kernel for the  $i$ -th bin, which is expressed as

$$W_{\text{g}}^i(z) = b_{\text{g}}^i(z) n_{\text{g}}^i(z). \quad (6)$$

Here  $b_{\text{g}}^i(z)$  is the galaxy bias, and the fiducial value is calculated by  $b_{\text{g}}^i(z) = 1 + 0.84 z_{\text{cen}}^i$ , where  $z_{\text{cen}}^i$  is the central redshift of the  $i$ -th bin (D. H. Weinberg et al. 2004). In the fitting process, we set it as a free parameter in each tomographic bin.  $n_{\text{g}}^i(z)$  is the normalized galaxy redshift distribution in the  $i$ -th bin, which has  $\int n_{\text{g}}^i(z) dz = 1$ .

To estimate  $n_{\text{g}}^i(z)$ , we assume that the total galaxy redshift distribution in the CSST photometric survey follows the function as (H. Lin et al. 2022)

$$n_{\text{g}}(z) \propto z^2 e^{-z/z^*}. \quad (7)$$

Here  $z^* = z_{\text{peak}}/2 = 0.3$ , where the distribution peak is  $z_{\text{peak}} = 0.6$ . Following Y. Gong et al. (2019), to utilize more information from the data, the redshift range is divided into four photometric tomographic bins, and we set the redshift bias  $\Delta z^i = 0$  and redshift scatter  $\sigma_z^i = 0.05$  as the fiducial values for each tomographic

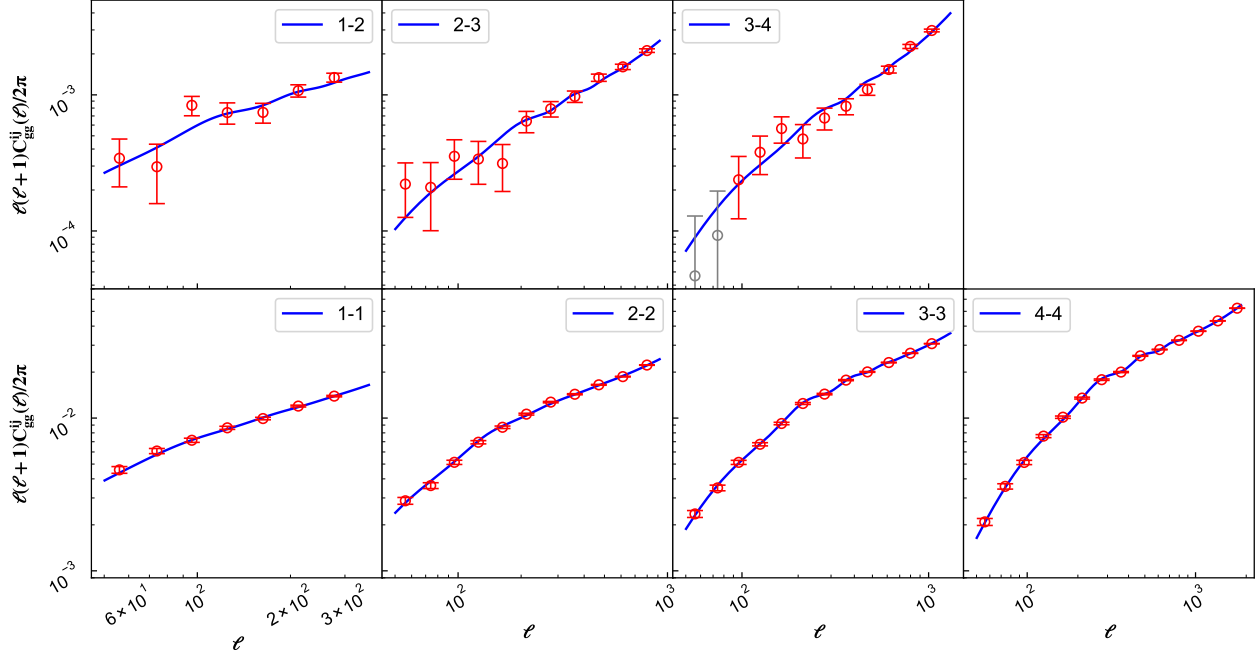


**Figure 3.** The theoretical curves and mock data of the galaxy angular power spectra in different tomographic bins for the CSST 3×2pt analysis. The blue solid curves represent the fiducial theoretical predictions. The red data points show the mock data used, while the gray data points indicate the excluded data with the signal-to-noise ratio (SNR) < 1. Due to the flat sky assumption, Limber approximation and to avoid nonlinear effects, we have set lower and upper limits on  $\ell$  for different redshift tomography bins. The galaxy cross-power spectra of different tomographic bins with low amplitudes and small overlapping redshift ranges of  $n_g^i(z)$  are also removed.

bin. These parameters are treated as free parameters during the fitting process.

In Figure 2, we show the adopted galaxy redshift distributions. The black dotted curve denotes the total galaxy redshift distribution  $n_g(z)$ , and it is normalized with  $\int n_g(z)dz = 1$ . The colored curves are the galaxy redshift distributions for the four tomographic bins. We find that the mean galaxy surface number densities in the four bins are  $\bar{n}_g^i = 7.9, 11.5, 4.6, 3.7 \text{ arcmin}^{-2}$ , respectively, and the corresponding total number density is  $\bar{n}_g = 27.7 \text{ arcmin}^{-2}$  which is consistent with the previous studies (e.g. Y. Gong et al. 2019). In Figure 3, the blue solid curves denote the theoretical galaxy angular auto- and cross-power spectra for different tomographic bins in the CSST photometric survey.

### 2.3. Shear Power Spectrum

The shear auto- or cross-power spectra measured by the CSST for the  $i$ -th and  $j$ -th bins can be estimated by (e.g. D. Huterer et al. 2006)

$$\tilde{C}_{\gamma\gamma}^{ij}(\ell) = (1 + m_i)(1 + m_j)C_{\gamma\gamma}^{ij}(\ell) + \delta_{ij}\frac{\sigma_\gamma^2}{\bar{n}_g^i} + N_{\text{add}}^\gamma, \quad (8)$$

where  $\delta_{ij}\sigma_\gamma^2/\bar{n}_g^i$  represents the shape shot noise term,  $\sigma_\gamma^2 = 0.04$  is the shear variance (Y. Gong et al. 2019).

The quantity  $m_i$  denotes the parameter for the multiplicative error in the  $i$ -th bin. The term  $N_{\text{add}}^\gamma$  is the additive error, which are simply assumed to be independent of bins or scales. We set  $m_i = 0$  and  $N_{\text{add}}^\gamma = 10^{-9}$  as the fiducial values (Y. Gong et al. 2019). The shear signal power spectrum is  $C_{\gamma\gamma}^{ij}(\ell)$ , which is given by (H. Hildebrandt et al. 2017)

$$C_{\gamma\gamma}^{ij} = P_\kappa^{ij}(\ell) + C_{\text{II}}^{ij}(\ell) + C_{\text{GI}}^{ij}(\ell), \quad (9)$$

where  $P_\kappa^{ij}(\ell)$  is the convergence power spectrum, which is the desired signal for cosmological analysis,  $C_{\text{II}}^{ij}(\ell)$  is Intrinsic-Intrinsic power spectrum, which comes from the correlation between the intrinsic ellipticities of two galaxies.  $C_{\text{GI}}^{ij}(\ell)$  is the Gravitational-Intrinsic power spectrum, which arises from the correlations between the gravitational shear of one galaxy and the intrinsic shape of another galaxy (B. Joachimi et al. 2015).

Assuming a flat sky and the Limber approximation (D. N. Limber 1954), the convergence power spectrum  $P_\kappa^{ij}(\ell)$  is given by (W. Hu & B. Jain 2004)

$$P_\kappa^{ij}(\ell) = \int dz H(z) \frac{W_\kappa^i(z)W_\kappa^j(z)}{cD_A^2(z)} P_m\left(\frac{\ell + \frac{1}{2}}{D_A(z)}, z\right), \quad (10)$$

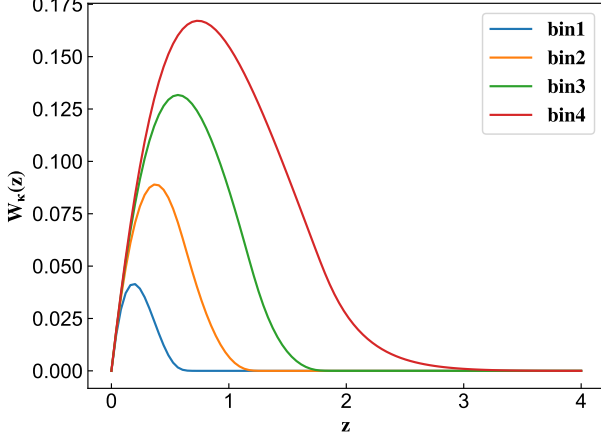


**Figure 4.** The weighting functions of the CSST weak lensing survey for the four tomographic bins.

where  $W_\kappa^i(z)$  is the lensing kernel function of the  $i$ -th bin, and it can be estimated by

$$W_\kappa^i(z) = \frac{3\Omega_m H_0^2 D_A(z)}{2cH(z)a} \int_z^\infty dz' n_g^i(z') \frac{D_A(z, z')}{D_A(z')}. \quad (11)$$

Here the integration limits are from  $z = 0$  to 4. Figure 4 shows the lensing weighting kernels for the four bins. We can see that  $W_\kappa^i(z)$  of the high-redshift bins can cover the low-redshift bins, which have wider distributions compared to  $W_\kappa^i(z)$  of the low-redshift bins.

The Intrinsic-Intrinsic power spectrum  $C_{\text{II}}^{ij}(\ell)$  is given by (H. Hildebrandt et al. 2017)

$$C_{\text{II}}^{ij} = \int dz H(z) \frac{F^i(z) F^j(z)}{cD_A^2(z)} P_m\left(\frac{\ell+1/2}{D_A(z)}, z\right), \quad (12)$$

$$F^i(z) = A_{\text{IA}} C_1 \rho_c \frac{\Omega_m}{D(z)} n_g^i(z) \left(\frac{1+z}{1+z_0}\right)^{\eta_{\text{IA}}} \left(\frac{L_i}{L_0}\right)^{\beta_{\text{IA}}}.$$

Here  $F^i(z)$  is the weighting kernel of the intrinsic alignment effect, the constant  $C_1 = 5 \times 10^{-14} h^{-2} M_\odot^{-1} \text{Mpc}^3$ ,  $\rho_c$  represents the present critical density,  $D(z)$  is the linear growth factor,  $z_0$  and  $L_0$  are the pivot redshift and luminosity, and  $A_{\text{IA}}$ ,  $\eta_{\text{IA}}$  and  $\beta_{\text{IA}}$  are free parameters. In this study, we adopt  $z_0 = 0.6$  and set the fiducial values  $A_{\text{IA}} = 1$  and  $\eta_{\text{IA}} = 0$  (H. Hildebrandt et al. 2017). For simplicity, we do not consider the luminosity dependence and fix  $\beta_{\text{IA}} = 0$  (Y. Gong et al. 2019; H. Lin et al. 2022).

The Gravitational-Intrinsic power spectrum consists of two components, representing the cross-correlation between gravitational lensing and intrinsic alignment for the  $i$ -th and  $j$ -th bins, which can be estimated by

$$C_{\text{GI}}^{ij} = \frac{1}{c} \int dz H(z) D_A^{-2}(z) [W^i(z) F^j(z) + W^j(z) F^i(z)] P_m\left(\frac{\ell+1/2}{D_A(z)}, z\right). \quad (13)$$

We find that the relationship  $C_{\gamma\gamma} > C_{\text{GI}} > C_{\text{II}}$  holds, and the effect of PBHs becomes significant when  $l \gtrsim 10^3$ . In Figure 5, the blue solid curves denote the theoretical shear angular auto- and cross-power spectra for different tomographic bins in the CSST photometric survey.

#### 2.4. Galaxy-Galaxy Lensing Power Spectrum

The galaxy-galaxy lensing power spectrum represents the cross correlation between the galaxy and weak lensing. It is expressed as (T. Abbott et al. 2018)

$$C_{g\gamma}^{ij}(\ell) = C_{g\kappa}^{ij}(\ell) + C_{g\text{I}}^{ij}(\ell). \quad (14)$$

The first term corresponds to the cross-correlation between galaxies and cosmic shear, and the second term is for the cross-correlation between galaxies and intrinsic alignment. The expressions for  $C_{g\kappa}^{ij}(\ell)$  and  $C_{g\text{I}}^{ij}(\ell)$  are

$$C_{g\kappa}^{ij}(\ell) = \int dz H(z) \frac{W_g^i(z) W_\kappa^j(z)}{cD_A^2(z)} P_m\left(\frac{\ell+1/2}{D_A(z)}, z\right), \quad (15)$$

$$C_{g\text{I}}^{ij}(\ell) = \int dz H(z) \frac{W_g^i(z) F^j(z)}{cD_A^2(z)} P_m\left(\frac{\ell+1/2}{D_A(z)}, z\right).$$

Since the cross-correlation between galaxy and cosmic shear  $C_{g\kappa}^{ij}(\ell)$  exceeds that between galaxy and intrinsic alignment  $C_{g\text{I}}^{ij}(\ell)$ ,  $C_{g\kappa}^{ij}(\ell)$  dominates the total signal. We find that the effect of PBHs becomes significant when  $l \gtrsim 10^3$ . In Figure 6, the blue solid curves denote the theoretical galaxy-galaxy lensing power spectra for different tomographic bins in the CSST photometric survey.

### 3. MOCK DATA

To generate the mock data of the CSST  $3 \times 2$ pt probe, the covariance matrix is needed, which can be estimated by (W. Hu & B. Jain 2004)

$$\text{Cov}[\tilde{C}_{xy}^{ab}(\ell) \tilde{C}_{mn}^{ij}(\ell')] = \frac{\delta_{\ell\ell'}}{(2\ell+1)f_{\text{sky}}\Delta\ell} [\tilde{C}_{xm}^{ai}(\ell) \tilde{C}_{yn}^{bj}(\ell) + \tilde{C}_{xn}^{aj}(\ell) \tilde{C}_{ym}^{bi}(\ell)], \quad (16)$$

where  $a, b, i, j \in \{1, 2, 3, 4\}$  denote different tomographic bins, and  $x, y, m, n \in \{g, \gamma\}$  denote galaxy or shear.  $f_{\text{sky}} \simeq 0.42$  is the sky fraction for the CSST wide-field survey. The covariance matrix is decomposed using Cholesky decomposition. Then, it is multiplied by a standard normal random matrix. This yields a random displacement matrix with the same covariance. The random displacement data are added to the  $3 \times 2$ pt theoretical predictions and forms the  $3 \times 2$ pt mock observed data. The mock data points of the CSST galaxy, weak lensing, and galaxy-lensing power spectra are shown in Figure 3, Figure 5, and Figure 6, respectively. The error



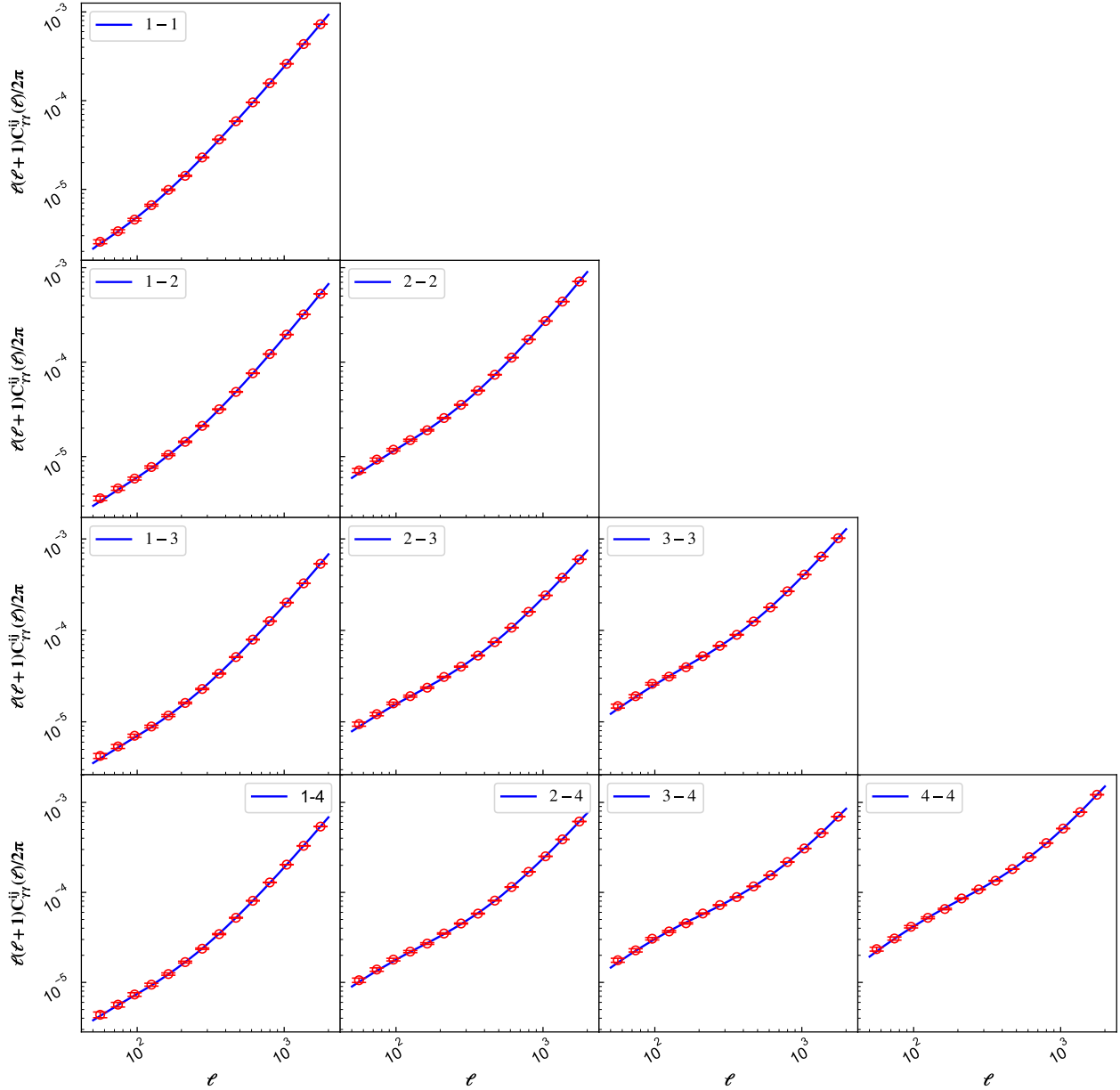


**Figure 5.** The theoretical curves and mock data of the shear angular power spectra for the CSST 3×2pt analysis. The blue solid curves are from the fiducial theoretical models. The red data points show the mock data used. Due to the flat sky assumption and Limber approximation, we have set lower limit on  $\ell$  for different redshift tomography bins.

bars of the data points in these figures are derived from the diagonal components of the covariance matrix.

Since the flat sky assumption and Limber approximation are only valid at  $\ell \gtrsim 50$  (D. N. Limber 1954), the data points of the angular power spectra at  $\ell < 50$  are discarded in the fitting process. Besides, we only adopt the data points with  $\text{SNR} > 1$  to improve the data quality and reduce computational time. The data points at small scales in the non-linear regime with  $k > 0.3 \text{ Mpc}^{-1}h$  are also removed in the galaxy and galaxy-lensing power spectra, which corresponds to

$l_{\text{max}} = 359, 920, 1316, 1891$  (H. Lin et al. 2022). For the shear power spectra, we take  $l_{\text{max}} = 2000$ . In addition, we also discard the cross power spectra of different tomographic bins for galaxies and shear signals with low amplitudes in Figure 3 and Figure 6, which have small overlapping redshift ranges for  $n_g^i(z)$ , or  $n_g^i(z)$  and  $W_\kappa^i(z)$ , as shown in Figure 2 and Figure 4.

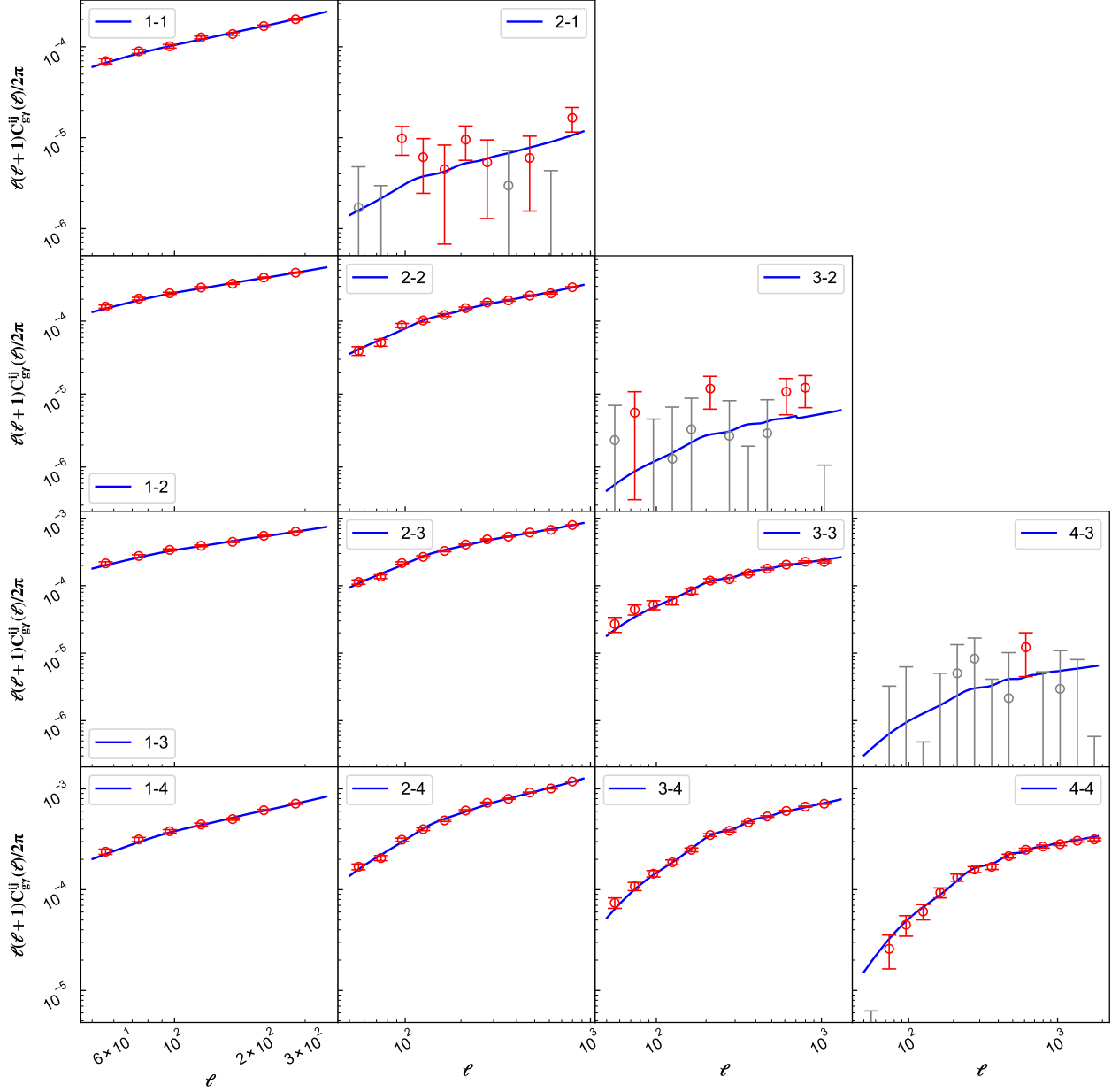


**Figure 6.** The theoretical curves and mock data of the galaxy-galaxy lensing angular power spectra in different tomographic bins for the CSST 3×2pt analysis. The blue solid curves represent the fiducial theoretical predictions. The red data points show the mock data used, while the gray data points indicate the excluded data with the SNR < 1. Due to the flat sky assumption, Limber approximation and to avoid nonlinear effects, we have set lower and upper limits on  $\ell$  for different redshift tomography bins. The galaxy-galaxy lensing cross-power spectra of different tomographic bins with low amplitudes and small overlapping redshift ranges of  $n_g^i(z)$  and  $W_\kappa^i(z)$  are also removed.

#### 4. CONSTRAINT AND RESULTS

##### 4.1. Fitting Method

We adopt the  $\chi^2$  method to fit the mock data, which is given by

$$\chi^2 = [\mathbf{D} - \mathbf{T}]^T \mathbf{Cov}^{-1} [\mathbf{D} - \mathbf{T}], \quad (17)$$

where  $\mathbf{D}$  represents the 3×2pt data vector,  $\mathbf{T}$  is the corresponding theoretical prediction vector, and  $\mathbf{Cov}$  is the

corresponding covariance matrix. The likelihood function follows  $\mathcal{L} \sim \exp(-\chi^2/2)$ .

The fitting process uses the `emcee` (D. Foreman-Mackey et al. 2013) package, which implements a Markov Chain Monte Carlo (MCMC) ensemble sampler. In Table 1, we summarize the free parameters, their fiducial values and priors for the CSST galaxy clustering, weak lensing, and 3×2pt surveys. The PBH

**Table 1.** The fiducial values, priors, best-fitting values and  $1\sigma$  errors of the free parameters in the CSST photometric surveys. The uniform and Gaussian priors are denoted by  $U(a, b)$  and  $N(\mu, \sigma)$ , respectively, where  $a$  and  $b$  are the prior range and  $\mu$  and  $\sigma$  are the mean and standard deviation. The relative accuracy for each parameter is also provided in brackets.

Parameter	Fiducial Value	Prior	Constraints by Galaxy Clustering	Constraints by Weak Lensing	Constraints by $3 \times 2$ pt
<b>Cosmological Parameter</b>					
$\Omega_m$	0.32	$U(0.2, 0.4)$	$0.334^{+0.030}_{-0.031}$ (9.2%)	$0.312^{+0.026}_{-0.025}$ (8.2%)	$0.313^{+0.011}_{-0.010}$ (3.3%)
$\Omega_b$	0.048	$U(0.01, 0.09)$	$0.0505^{+0.0068}_{-0.0068}$ (13%)	$0.040^{+0.014}_{-0.014}$ (34%)	$0.0500^{+0.0028}_{-0.0028}$ (5.6%)
$h$	0.6727	$N(0.6727, 0.0060)$	$0.6732^{+0.0057}_{-0.0058}$ (0.85%)	$0.6731^{+0.0059}_{-0.0060}$ (0.89%)	$0.6729^{+0.0055}_{-0.0058}$ (0.84%)
$n_s$	0.96	$U(0.85, 1.15)$	$0.947^{+0.039}_{-0.038}$ (4.0%)	$0.927^{+0.049}_{-0.048}$ (5.2%)	$0.980^{+0.020}_{-0.022}$ (2.1%)
$w$	-1	$U(-1.5, 0.8)$	$-1.10^{+0.20}_{-0.25}$ (21%)	$-1.10^{+0.18}_{-0.13}$ (14%)	$-1.20^{+0.15}_{-0.17}$ (13%)
$\sigma_8$	0.8	$U(0.7, 0.9)$	$0.790^{+0.037}_{-0.031}$ (4.3%)	$0.804^{+0.021}_{-0.022}$ (2.6%)	$0.805^{+0.015}_{-0.012}$ (1.7%)
$\log_{10}(f_{\text{PBH}} m_{\text{PBH}}/M_\odot + 1)$	0	$U[0, 8]$	$< 4.6$	$< 4.1$	$< 3.9$
<b>Baryonic Effect</b>					
$\log_{10}(T_{\text{AGN}}/K)$	7.8	$U(7.0, 8.3)$	$7.53^{+0.43}_{-0.35}$ (5.2%)	$7.60^{+0.17}_{-0.13}$ (2.0%)	$7.756^{+0.094}_{-0.093}$ (1.2%)
<b>Intrinsic Alignment</b>					
$A_{\text{IA}}$	1	$U(-5, 5)$	—	$1.04^{+0.23}_{-0.17}$ (19%)	$0.968^{+0.041}_{-0.036}$ (4.0%)
$\eta_{\text{IA}}$	0	$U(-5, 5)$	—	$-0.03^{+0.82}_{-0.72}$	$0.144^{+0.085}_{-0.087}$
<b>Galaxy Bias</b>					
$b^1$	1.252	$U(0, 5)$	$1.221^{+0.071}_{-0.068}$	—	$1.242^{+0.022}_{-0.024}$
$b^2$	1.756	$U(0, 5)$	$1.777^{+0.069}_{-0.076}$	—	$1.767^{+0.037}_{-0.036}$
$b^3$	2.260	$U(0, 5)$	$2.31^{+0.10}_{-0.10}$	—	$2.306^{+0.062}_{-0.061}$
$b^4$	3.436	$U(0, 5)$	$3.49^{+0.18}_{-0.18}$	—	$3.50^{+0.11}_{-0.11}$
<b>Photo-<math>z</math> Calibration</b>					
$\Delta z^1$	0	$U(-0.1, 0.1)$	$-0.027^{+0.047}_{-0.040}$	$-0.000^{+0.022}_{-0.034}$	$-0.0074^{+0.0077}_{-0.0097}$
$\Delta z^2$	0	$U(-0.1, 0.1)$	$-0.018^{+0.040}_{-0.035}$	$0.005^{+0.026}_{-0.036}$	$-0.0073^{+0.0081}_{-0.0010}$
$\Delta z^3$	0	$U(-0.1, 0.1)$	$-0.011^{+0.041}_{-0.038}$	$0.004^{+0.036}_{-0.034}$	$-0.008^{+0.011}_{-0.014}$
$\Delta z^4$	0	$U(-0.1, 0.1)$	$-0.010^{+0.052}_{-0.046}$	$0.023^{+0.052}_{-0.055}$	$-0.016^{+0.017}_{-0.018}$
$\sigma_z^1/\sigma_{z,\text{fid}}^1$	1	$U(0.5, 1.5)$	$1.00^{+0.32}_{-0.33}$	$1.05^{+0.31}_{-0.36}$	$1.0^{+0.1}_{-0.1}$
$\sigma_z^2/\sigma_{z,\text{fid}}^2$	1	$U(0.5, 1.5)$	$1.02^{+0.32}_{-0.35}$	$1.06^{+0.31}_{-0.33}$	$0.957^{+0.060}_{-0.074}$
$\sigma_z^3/\sigma_{z,\text{fid}}^3$	1	$U(0.5, 1.5)$	$1.03^{+0.31}_{-0.34}$	$0.99^{+0.35}_{-0.33}$	$0.976^{+0.095}_{-0.093}$
$\sigma_z^4/\sigma_{z,\text{fid}}^4$	1	$U(0.5, 1.5)$	$0.87^{+0.52}_{-0.47}$	$0.97^{+0.34}_{-0.33}$	$0.82^{+0.25}_{-0.20}$
<b>Shear Calibration and Noise</b>					
$m_1$	0	$U(-0.1, 0.1)$	—	$0.008^{+0.054}_{-0.055}$	$0.027^{+0.037}_{-0.036}$
$m_2$	0	$U(-0.1, 0.1)$	—	$0.011^{+0.050}_{-0.054}$	$0.019^{+0.032}_{-0.033}$
$m_3$	0	$U(-0.1, 0.1)$	—	$0.013^{+0.048}_{-0.052}$	$0.021^{+0.032}_{-0.033}$
$m_4$	0	$U(-0.1, 0.1)$	—	$0.010^{+0.047}_{-0.054}$	$0.023^{+0.032}_{-0.033}$
$N_{\text{sys}}^g$	$10^{-8}$	$U(0.5, 1.5) \times 10^{-8}$	$1.063^{+0.043}_{-0.042} \times 10^{-8}$	—	$9.93^{+0.26}_{-0.28} \times 10^{-9}$
$N_{\text{add}}^\gamma$	$10^{-9}$	$U(0.5, 1.5) \times 10^{-9}$	—	$9.987^{+0.027}_{-0.025} \times 10^{-10}$	$1.0032^{+0.0021}_{-0.0024} \times 10^{-9}$
$N_{\text{add}}^{g\gamma}$	0	$U(-1, 1) \times 10^{-8}$	—	—	$0.1^{+1.4}_{-1.4} \times 10^{-11}$

parameter  $f_{\text{PBH}} m_{\text{PBH}}$  spans nearly ten orders of magnitude, and thus its logarithmic form is taken, i.e.  $\log_{10}(f_{\text{PBH}} m_{\text{PBH}}/M_\odot + 1)$  as the constraint parameter. The MCMC implementation uses 150 walkers with 22,000 steps each to ensure the convergence. After burn-in and thinning process, approximately 10,000 chain points remain to illustrate the 1D probability distribu-

tion functions (PDFs) and contour maps of the free parameters.

#### 4.2. Constraint result

In Figure 7, the contour maps and 1D PDFs for the PBH, cosmological, and baryonic effect parameters have been shown. The  $1\sigma$  constraint result and the relative constraint accuracy for each parameter from the CSST



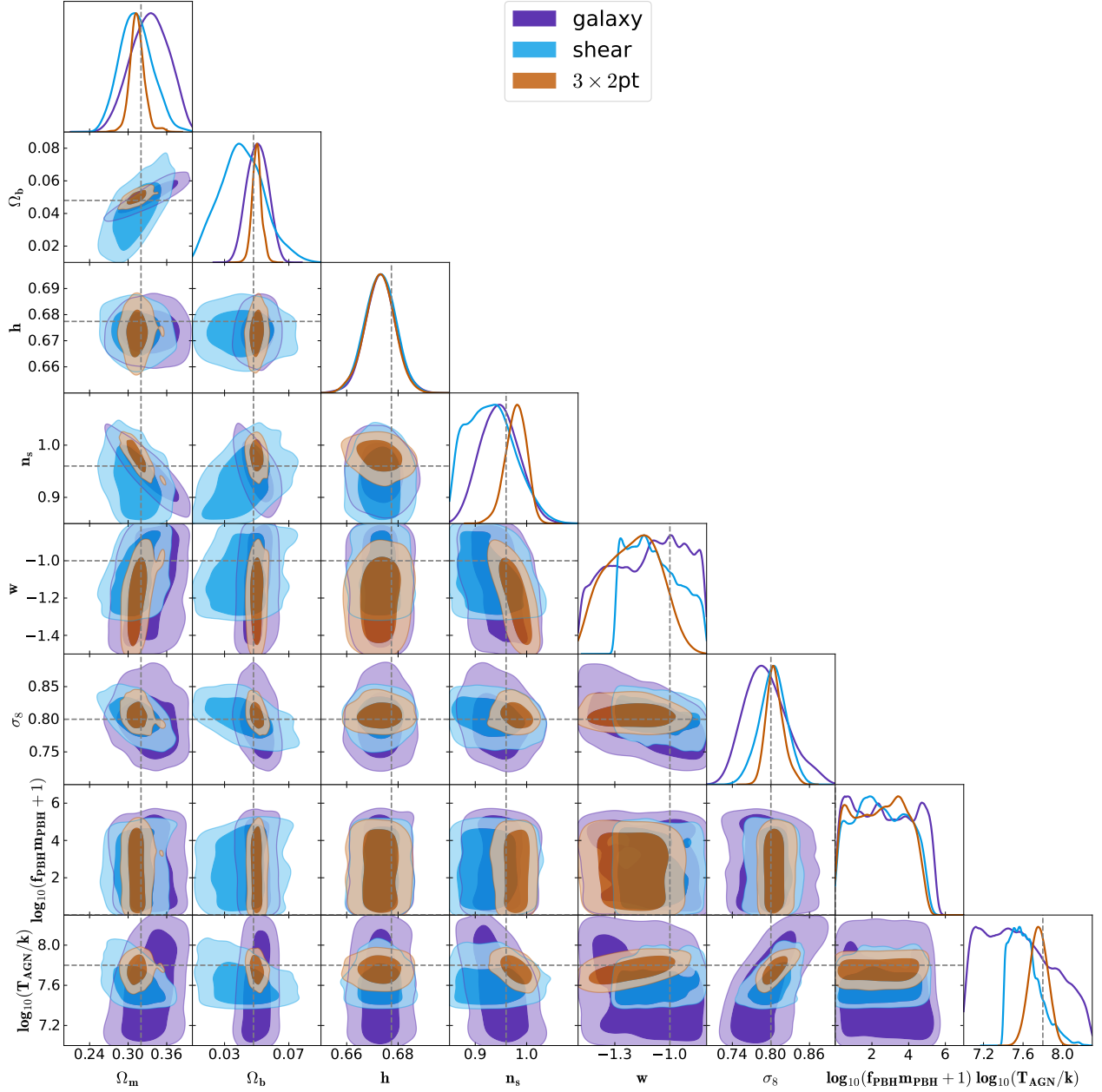


**Figure 7.** The contour maps with  $1\sigma$  (68%) and  $2\sigma$  (95%) CLs and 1D PDFs of the cosmological, PBH, and baryonic effect parameters for the CSST galaxy clustering (purple), cosmic shear (blue) and  $3\times 2$ pt (brown) surveys. The gray vertical and horizontal dashed lines indicate the fiducial values of these parameters.

galaxy clustering, weak lensing, and  $3\times 2$ pt surveys are listed in Table 1.

We can find that, due to the large sky area and redshift coverage of the CSST photometric survey, the constraint accuracies of the PBH parameter product  $f_{\text{PBH}}m_{\text{PBH}}$  can reach  $< 10^{3.9}M_{\odot}$  and  $< 10^{4.7}M_{\odot}$  for  $1\sigma$  and  $2\sigma$  confidence levels (CLs), respectively. We also notice that the constraint on the product  $f_{\text{PBH}}m_{\text{PBH}}$  from the CSST  $3\times 2$ pt analysis is similar to that from the CSST weak lensing survey, which indicates that the constraint

power is mainly provided by the CSST shear measurement covering the small scales.

In Figure 8, we show the comparison of the constraint on  $f_{\text{PBH}}$  as a function of  $m_{\text{PBH}}$  with other results, based on our  $2\sigma$  upper limit with  $f_{\text{PBH}}m_{\text{PBH}} < 10^{4.7}M_{\odot}$ . The filled regions represent the excluded parameter space. In the mass range  $m_{\text{PBH}} \gtrsim 10^8 M_{\odot}$ , we can see that the CSST  $3\times 2$ pt analysis can provide tighter constraints than other current methods, such as HST, LSSF, DH, and CMB, especially in the mass range

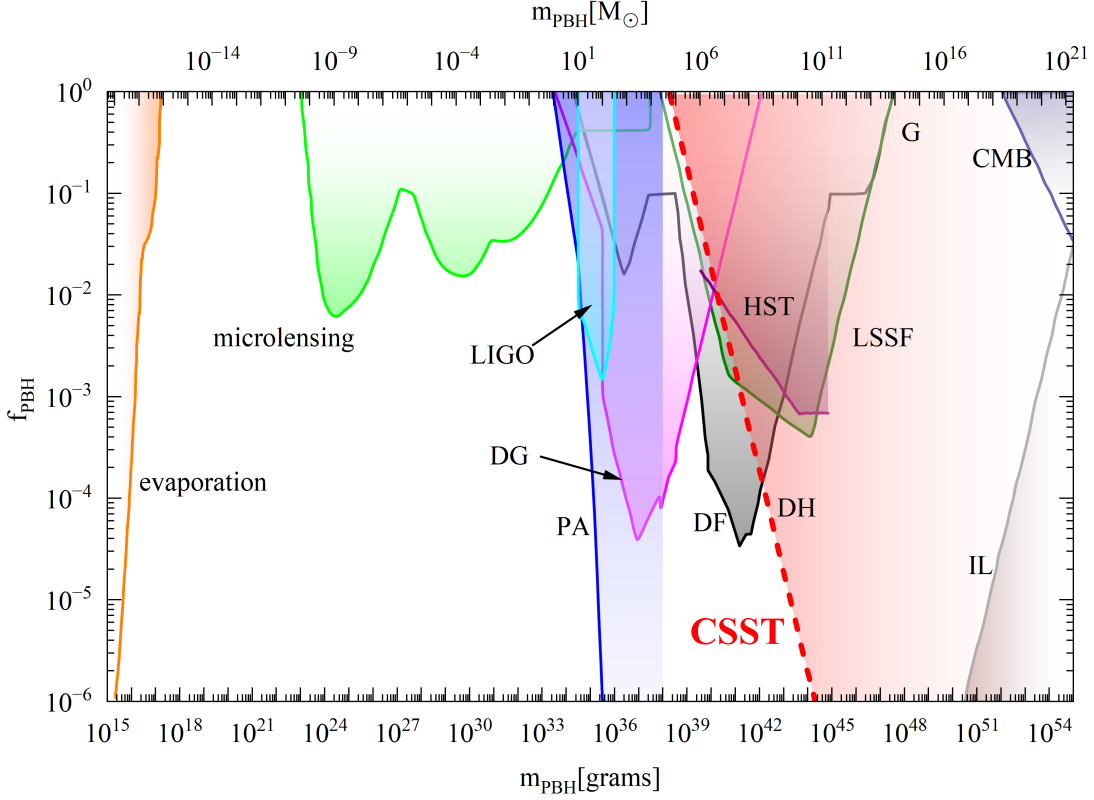


**Figure 8.** Comparison of the constraints on the monochromatic mass function  $f_{\text{PBH}}(m_{\text{PBH}})$ . The filled regions represent the excluded parameter space. The red dash line is derived from the  $2\sigma$  upper limit ( $f_{\text{PBH}}m_{\text{PBH}} < 10^{4.7}M_{\odot}$ ) given by this work using the CSST  $3 \times 2$ pt analysis. The solid lines indicate various previous constraints, including the limits from evaporation (orange), microlensing (green), Planck measurements of CMB distortions (PA, blue), halo dynamical friction (DF, black), heating of stars in the Galactic disk (DH, black), galaxy tidal distortions (G, black), large-scale structure formation limits requiring that structures do not form too early (LSSF, olive green), CMB dipole (CMB, navy blue), and incredulity limits (IL, burgundy) (B. Carr & F. Kuhnel 2020). Additional constraints come from LIGO observation of the merger rate of PBH binaries (LIGO, cyan) (Y. Ali-Haïmoud et al. 2017), PBH in the halos of dwarf galaxies (DG, magenta) (S. V. Pilipenko et al. 2025), and measurements of the galaxy UV luminosity functions by the Hubble Space Telescope (HST, purple) (Y. Gouttenoire et al. 2024).

$10^{14}M_{\odot} < m_{\text{PBH}} < 10^{18}M_{\odot}$  where currently no effective constraints. Therefore, it demonstrates strong potential for the future studies of massive PBHs using the CSST  $3 \times 2$ pt analysis.

For the cosmological parameters, e.g.  $\Omega_m$ ,  $\sigma_8$ , and  $w$ , we find that the CSST  $3 \times 2$ pt analysis can provide the constraint accuracies  $\sim 3.3\%$ ,  $1.7\%$ , and  $13\%$ , respectively, which are much more stringent than those given by the current similar surveys, e.g. DES (D. E. S. Collaboration et al. 2022). Compared with the previous CSST  $3 \times 2$ pt forecast (e.g. H. Lin et al. 2022, 2024), we notice that the values of relative constraint accuracies of these parameters are larger. This is mainly because that we have included more parameters in this analysis, such as the noise parameters  $N_{\text{sys}}^g$ ,  $N_{\text{add}}^g$ , and  $N_{\text{add}}^{g\gamma}$ .

In addition, we find that the systematical parameters are also correctly constrained in the CSST photometric surveys, and their fiducial values are within the  $1\sigma$  CL, such as the parameters of baryonic effect  $\log_{10}(T_{\text{AGN}}/k)$ ,

intrinsic alignment  $A_{\text{IA}}$  and  $\eta_{\text{IA}}$ , galaxy bias in each redshift bin  $b_g^i$ , photo- $z$  calibration in each redshift bin  $\Delta z^i$  and  $\sigma_z^i$ , shear calibration in each redshift bin  $m_i$ , and noise terms  $N_{\text{sys}}^g$ ,  $N_{\text{add}}^g$ , and  $N_{\text{add}}^{g\gamma}$ . A detailed discussion of these parameters is provided in appendix A.

## 5. SUMMARY

In this work, we forecast the constraint on the product of the PBH CDM fraction and mass, i.e.  $f_{\text{PBH}}m_{\text{PBH}}$ , and other cosmological parameters using the CSST  $3 \times 2$ pt analysis. The modeling incorporates PBH isocurvature perturbations and ordinary  $\Lambda$ CDM adiabatic perturbations to construct the total matter power spectrum and then generate the mock data of the angular power spectra of galaxy clustering, weak lensing, and galaxy-galaxy lensing based on the design of the CSST photometric survey. The systematic parameters of baryonic effect, intrinsic alignment, galaxy bias, photo- $z$  calibration, shear calibration, and noise terms, are also consid-

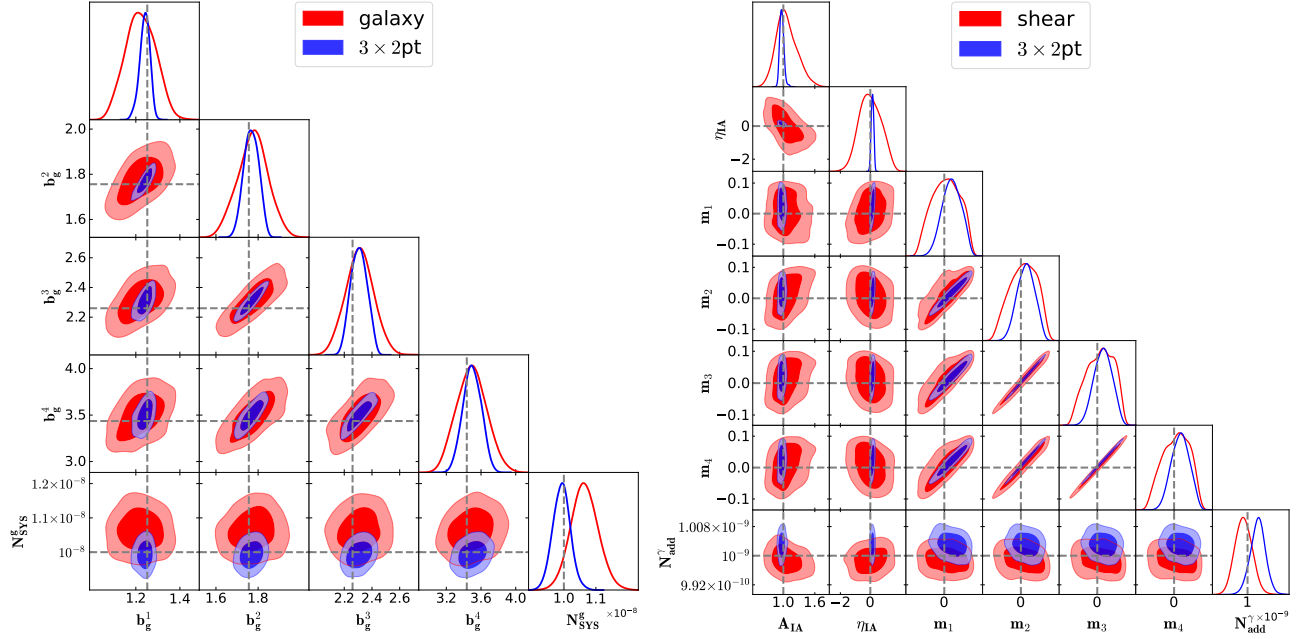


**Figure 9.** *Left panel:* The contour maps with  $1\sigma$  and  $2\sigma$  CLs and 1D PDFs of galaxy bias and systematic noise for the CSST galaxy clustering (red) and  $3 \times 2\text{pt}$  surveys (blue). *Right panel:* The contour maps with  $1\sigma$  and  $2\sigma$  CLs and 1D PDFs of intrinsic alignment, multiplicative and additive errors for the CSST shear (red) and  $3 \times 2\text{pt}$  surveys (blue). The gray vertical and horizontal dashed lines indicate the fiducial values of these parameters.

ered and jointly constrained in the MCMC fitting process.

We find that the CSST  $3 \times 2\text{pt}$  analysis can provide tight constraints on the PBH parameter with  $f_{\text{PBH}} m_{\text{PBH}} < 10^{3.9} M_\odot$  and  $< 10^{4.7} M_\odot$  for  $1\sigma$  and  $2\sigma$  CLs, respectively. It excludes significant portions of the parameter space in the mass range  $m_{\text{PBH}} > 10^8 M_\odot$ , especially for  $10^{14} M_\odot < m_{\text{PBH}} < 10^{18} M_\odot$  where the existing methods lack of sensitivity. We also notice that this constraint is mainly contributed by the CSST weak lensing measurement, which can provide more information at small scales. Besides, the constraints on the cosmological parameters, such as  $\Omega_m$ ,  $\sigma_8$ , and  $w$  can achieve much higher precision compared to the current photometric surveys, and the systematic parameters are also well-constrained. Our results validates the potential of the upcoming or ongoing Stage IV surveys for exploring the LSS evolution of the Universe, and indicates that the CSST  $3 \times 2\text{pt}$  analysis can be a powerful tool for investigating the properties of PBHs.

## APPENDIX

### A. CONSTRAINT RESULTS OF SYSTEMATIC PARAMETERS

The CSST photometric survey also can effectively constrain the systematic parameters in the model. In Figure 9, we show the contour maps and 1D PDFs of the parameters of galaxy bias, intrinsic alignment, multiplicative error, and noise terms in the CSST galaxy clustering, shear, and  $3 \times 2\text{pt}$  measurements. Compared to the galaxy clustering

### ACKNOWLEDGMENTS

D.A.H and Y.G. acknowledge the support from National Key R&D Program of China grant Nos. 2022YFF0503404 and 2020SKA0110402, and the CAS Project for Young Scientists in Basic Research (No. YSBR-092). X.L.C. acknowledges the support of the National Natural Science Foundation of China through grant Nos. 11473044 and 11973047 and the Chinese Academy of Science grants ZDKYYQ20200008, QYZDJ-SSW-SLH017, XDB 23040100, and XDA15020200. This work is also supported by science research grants from the China Manned Space Project with grant Nos. CMS-CSST-2025-A02, CMS-CSST-2021-B01, and CMS-CSST-2021-A01.

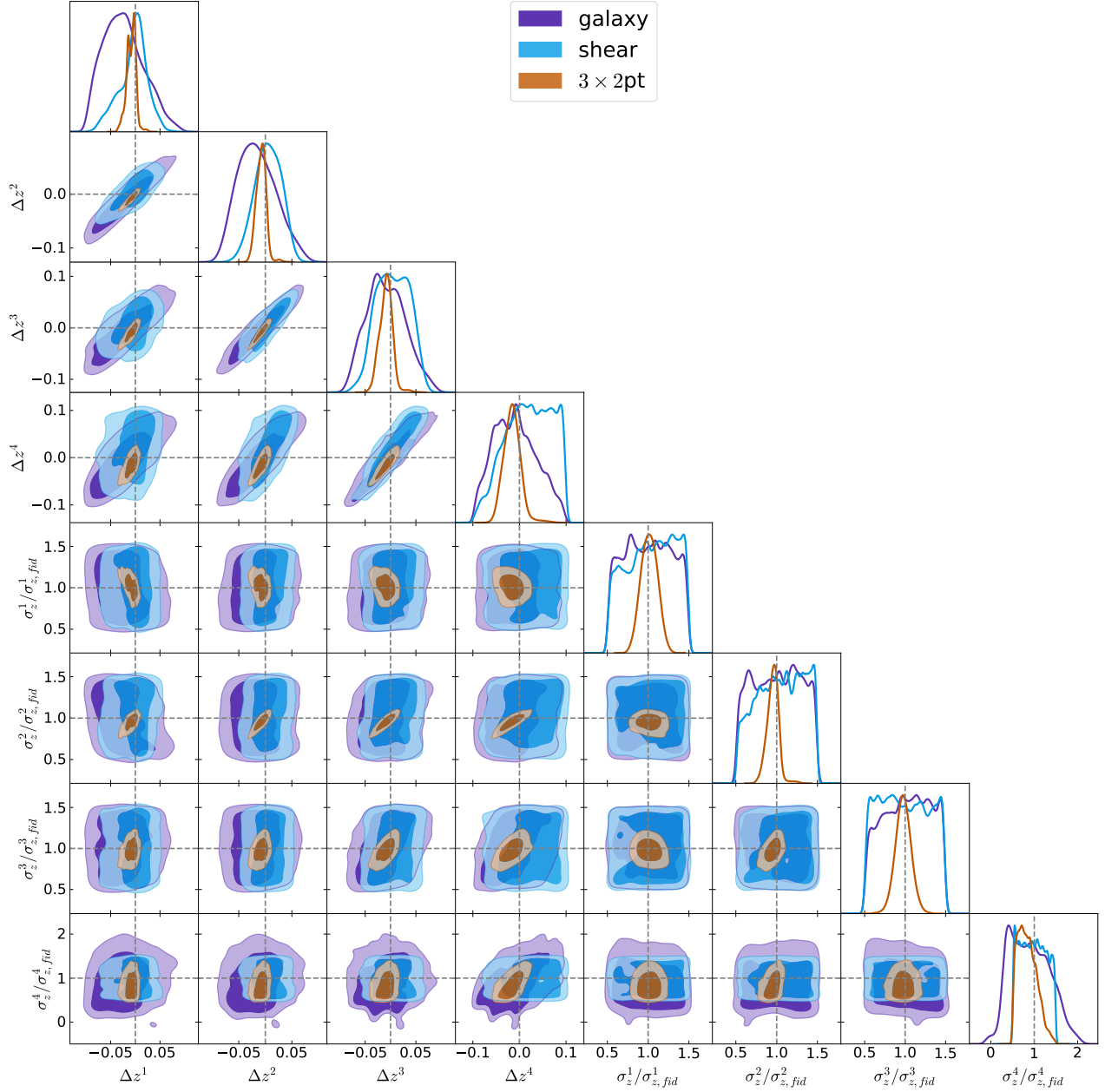


**Figure 10.** The contour maps with  $1\sigma$  and  $2\sigma$  CLs and 1d PDFs of the systematic parameters in the photo- $z$  calibration for the CSST galaxy clustering (purple), cosmic shear (blue) and  $3 \times 2$ pt (brown) surveys. The gray vertical and horizontal dashed lines indicate the fiducial values of these parameters.

measurement, the  $3 \times 2$ pt analysis can improve the constraint accuracies of the galaxy bias and shot noise by a factor of  $\sim 2$ . For the intrinsic alignment parameters, the  $3 \times 2$ pt method demonstrates a significant advantage in constraining  $A_{IA}$ , improving the constraint accuracy by a factor of  $\sim 5$ . In Figure 10, we show the contour maps and 1D PDFs of the systematic parameters in photo- $z$  calibration, i.e.  $\Delta z^i$  and  $\sigma_z^i$ . Compared to the results from the CSST galaxy clustering only and shear only measurements, the CSST  $3 \times 2$ pt survey can improve the constraint accuracy by a factor of  $\sim 3$ .

## REFERENCES

- Abbott, T., Abdalla, F., Alarcon, A., & others. 2018, Physical Review D, 98, 043526, doi: [10.1103/PhysRevD.98.043526](https://doi.org/10.1103/PhysRevD.98.043526)
- Afshordi, N., McDonald, P., & Spergel, D. N. 2003, Astrophysical Journal, 594, L71, doi: [10.1086/378763](https://doi.org/10.1086/378763)

- Ali-Haimoud, Y., Kovetz, E. D., & Kamionkowski, M. 2017, *Physical Review D*, 96, 123523, doi: [10.1103/PhysRevD.96.123523](https://doi.org/10.1103/PhysRevD.96.123523)
- Arbey, A., Auffinger, J., & Silk, J. 2020, *Physical Review D*, 101, 023010, doi: [10.1103/PhysRevD.101.023010](https://doi.org/10.1103/PhysRevD.101.023010)
- Byrnes, C., Franciolini, G., Harada, T., Pani, P., & Sasaki, M., eds. 2025, *Primordial black holes*, Springer Series in Astrophysics and Cosmology (Singapore: Springer Nature Singapore), doi: [10.1007/978-981-97-8887-3](https://doi.org/10.1007/978-981-97-8887-3)
- Carr, B., Clesse, S., & García-Bellido, J. 2021a, *Monthly Notices of the Royal Astronomical Society*, 501, 1426, doi: [10.1093/mnras/staa3726](https://doi.org/10.1093/mnras/staa3726)
- Carr, B., Kohri, K., Sendouda, Y., & Yokoyama, J. 2021b, *Reports on Progress in Physics*, 84, 116902, doi: [10.1088/1361-6633/ac1e31](https://doi.org/10.1088/1361-6633/ac1e31)
- Carr, B., & Kuhnel, F. 2020, *Annual Review of Nuclear and Particle Science*, 70, 355, doi: [10.1146/annurev-nucl-050520-125911](https://doi.org/10.1146/annurev-nucl-050520-125911)
- Carr, B., Raidal, M., Tenkanen, T., Vaskonen, V., & Veermäe, H. 2017, *Physical Review D*, 96, 23514, doi: [10.1103/PhysRevD.96.023514](https://doi.org/10.1103/PhysRevD.96.023514)
- Carr, B., & Silk, J. 2018, *Monthly Notices of the Royal Astronomical Society*, 478, 3756, doi: [10.1093/mnras/sty1204](https://doi.org/10.1093/mnras/sty1204)
- Carr, B. J. 1975, *Astrophysical Journal*, 201, 1, doi: [10.1086/153853](https://doi.org/10.1086/153853)
- Carr, B. J., & Green, A. M. 2024, doi: [10.48550/arXiv.2406.05736](https://doi.org/10.48550/arXiv.2406.05736)
- Chen, A., Gong, Y., Wu, F., Wang, Y., & Chen, X. 2022, *Research in Astronomy and Astrophysics*, 22, 55021, doi: [10.1088/1674-4527/ac6418](https://doi.org/10.1088/1674-4527/ac6418)
- Collaboration, C., Gong, Y., Miao, H., et al. 2025, *Introduction to the chinese space station survey telescope (CSST)*, arXiv, doi: [10.48550/arXiv.2507.04618](https://doi.org/10.48550/arXiv.2507.04618)
- Collaboration, D. E. S., Abbott, T. M. C., Agüena, M., et al. 2022, *Physical Review D*, 105, 023520, doi: [10.1103/PhysRevD.105.023520](https://doi.org/10.1103/PhysRevD.105.023520)
- Collaboration, E., Blot, L., Tanidis, K., et al. 2025a, doi: [10.48550/arXiv.2510.10021](https://doi.org/10.48550/arXiv.2510.10021)
- Collaboration, E., Cañas-Herrera, G., Goh, L. W. K., et al. 2025b, doi: [10.48550/arXiv.2510.09153](https://doi.org/10.48550/arXiv.2510.09153)
- Collaboration, P., Aghanim, N., Akrami, Y., et al. 2020, *Astronomy and Astrophysics*, 641, A6, doi: [10.1051/0004-6361/201833910](https://doi.org/10.1051/0004-6361/201833910)
- Foreman-Mackey, D., Hogg, D. W., Lang, D., & Goodman, J. 2013, *Publications of the Astronomical Society of the Pacific*, 125, 306, doi: [10.1086/670067](https://doi.org/10.1086/670067)
- Gong, Y., Liu, X., Cao, Y., et al. 2019, *The Astrophysical Journal*, 883, 203, doi: [10.3847/1538-4357/ab391e](https://doi.org/10.3847/1538-4357/ab391e)
- Gong, Y., Miao, H., Zhou, X., et al. 2025, *Science China Physics, Mechanics & Astronomy*, 68, 280402, doi: [10.1007/s11433-025-2646-2](https://doi.org/10.1007/s11433-025-2646-2)
- Gouttenoire, Y., Trifinopoulos, S., Valogiannis, G., & Vanvlasselaer, M. 2024, *Phys. Rev. D*, 109, 123002, doi: [10.1103/PhysRevD.109.123002](https://doi.org/10.1103/PhysRevD.109.123002)
- Green, J., Schechter, P., Baltay, C., et al. 2012, *Wide-field InfraRed survey telescope (WFIRST) final report*, arXiv, doi: [10.48550/arXiv.1208.4012](https://doi.org/10.48550/arXiv.1208.4012)
- Hildebrandt, H., Viola, M., Heymans, C., et al. 2017, *Mon. Not. Roy. Astron. Soc.*, 465, 1454, doi: [10.1093/mnras/stw2805](https://doi.org/10.1093/mnras/stw2805)
- Hu, W., & Jain, B. 2004, *Physical Review D*, 70, 043009, doi: [10.1103/PhysRevD.70.043009](https://doi.org/10.1103/PhysRevD.70.043009)
- Huterer, D., Takada, M., Bernstein, G., & Jain, B. 2006, *Monthly Notices of the Royal Astronomical Society*, 366, 101, doi: [10.1111/j.1365-2966.2005.09782.x](https://doi.org/10.1111/j.1365-2966.2005.09782.x)
- Inman, D., & Ali-Haimoud, Y. 2019, *Physical Review D*, 100, 083528, doi: [10.1103/PhysRevD.100.083528](https://doi.org/10.1103/PhysRevD.100.083528)
- Ivezic, Z., Kahn, S. M., Tyson, J. A., et al. 2019, *The Astrophysical Journal*, 873, 111, doi: [10.3847/1538-4357/ab042c](https://doi.org/10.3847/1538-4357/ab042c)
- Joachimi, B., Cacciato, M., Kitching, T. D., et al. 2015, *Space Science Reviews*, 193, 1, doi: [10.1007/s11214-015-0177-4](https://doi.org/10.1007/s11214-015-0177-4)
- Kashlinsky, A., Arendt, R. G., Ashby, M. L. N., Kruk, J., & Odegard, N. 2025, 980, L12, doi: [10.3847/2041-8213/adad5e](https://doi.org/10.3847/2041-8213/adad5e)
- Kühnel, F., Rampf, C., & Sandstad, M. 2016, *The European Physical Journal C*, 76, 93, doi: [10.1140/epjc/s10052-016-3945-8](https://doi.org/10.1140/epjc/s10052-016-3945-8)
- Lewis, A., Challinor, A., & Lasenby, A. 2000, *Astrophysical Journal*, 538, 473, doi: [10.1086/309179](https://doi.org/10.1086/309179)
- Limber, D. N. 1954, *Astrophysical Journal*, 119, 655, doi: [10.1086/145870](https://doi.org/10.1086/145870)
- Lin, H., Deng, F., Gong, Y., & Chen, X. 2024, *Mon. Not. Roy. Astron. Soc.*, 529, 1542, doi: [10.1093/mnras/stae627](https://doi.org/10.1093/mnras/stae627)
- Lin, H., Gong, Y., Chen, X., et al. 2022, *Monthly Notices of the Royal Astronomical Society*, 515, 5743, doi: [10.1093/mnras/stac2126](https://doi.org/10.1093/mnras/stac2126)
- Matteri, A., Ferrara, A., & Pallottini, A. 2025, *Beyond the first galaxies primordial black holes shine*, arXiv, doi: [10.48550/arXiv.2503.18850](https://doi.org/10.48550/arXiv.2503.18850)
- Mead, A., Brieden, S., Tröster, T., & Heymans, C. 2021, *Monthly Notices of the Royal Astronomical Society*, 502, 1401, doi: [10.1093/mnras/stab082](https://doi.org/10.1093/mnras/stab082)
- Miao, H., Gong, Y., Chen, X., et al. 2024, 531, 3991, doi: [10.1093/mnras/stae1370](https://doi.org/10.1093/mnras/stae1370)
- More, S., Sugiyama, S., Miyatake, H., et al. 2023, *Phys. Rev. D*, 108, 123520, doi: [10.1103/PhysRevD.108.123520](https://doi.org/10.1103/PhysRevD.108.123520)

- Pilipenko, S. V., Tkachev, M. V., & Arakelyan, N. R. 2025, doi: [10.48550/arXiv.2501.18239](https://doi.org/10.48550/arXiv.2501.18239)
- Serpico, P. D. 2024, CMB and accretion, arXiv. <http://arxiv.org/abs/2406.12489>
- Song, Y., Xiong, Q., Gong, Y., et al. 2024a, 532, 1049, doi: [10.1093/mnras/stae1575](https://doi.org/10.1093/mnras/stae1575)
- Song, Y., Xiong, Q., Gong, Y., et al. 2024b, 976, 244, doi: [10.3847/1538-4357/ad8de9](https://doi.org/10.3847/1538-4357/ad8de9)
- Stolzner, B., Wright, A. H., Asgari, M., et al. 2025, doi: [10.48550/arXiv.2503.19442](https://doi.org/10.48550/arXiv.2503.19442)
- Sugiyama, S., Miyatake, H., More, S., et al. 2023, Phys. Rev. D, 108, 123521, doi: [10.1103/PhysRevD.108.123521](https://doi.org/10.1103/PhysRevD.108.123521)
- Weinberg, D. H., Davé, R., Katz, N., & Hernquist, L. 2004, Astrophysical Journal, 601, 1, doi: [10.1086/380481](https://doi.org/10.1086/380481)
- Wright, A. H., Stolzner, B., Asgari, M., et al. 2025, doi: [10.48550/arXiv.2503.19441](https://doi.org/10.48550/arXiv.2503.19441)
- Xiong, Q., Gong, Y., Zhou, X., et al. 2024, Cosmological forecast for the weak gravitational lensing and galaxy clustering joint analysis in the CSST photometric survey, arXiv. <http://arxiv.org/abs/2410.19388>
- Yan, J.-H., Gong, Y., Wang, M., Miao, H., & Chen, X. 2024, Research in Astronomy and Astrophysics, 24, 115013, doi: [10.1088/1674-4527/ad86a7](https://doi.org/10.1088/1674-4527/ad86a7)
- Zhan, H. 2011, SCIENTIA SINICA Physica, Mechanica & Astronomica, 41, 1441, doi: [10.1360/132011-961](https://doi.org/10.1360/132011-961)
- Zhan, H. 2021, Chinese Science Bulletin, 66, 1290, doi: [10.1360/TB-2021-0016](https://doi.org/10.1360/TB-2021-0016)